

B20-MnSi films grown on Si(100) substrates with magnetic skyrmion signature

Zichao Li^{1,2*}, Ye Yuan^{1,3}, René Hübner¹, Viktor Begeza^{1,4}, Thomas Naumann¹, Lars Rebohle¹, Olav Hellwig^{1,5}, Manfred Helm^{1,4}, Kornelius Nielsch^{2,4,6}, Slawomir Prucnal¹, Shengqiang Zhou^{1*}

¹Helmholtz-Zentrum Dresden-Rossendorf, Institute of Ion Beam Physics and Materials Research, Bautzner Landstrasse 400, D-01328 Dresden, Germany

²Institute of Materials Science, Technische Universität Dresden, 01069 Dresden, Germany

³Songshan Lake Materials Laboratory, Dongguan, Guangdong 523808, People's Republic of China

⁴Institute of Applied Physics, Technische Universität Dresden, 01062 Dresden, Germany

⁵Institute of Physics, Chemnitz University of Technology, Chemnitz 09126, Germany

⁶Institute for Metallic Materials, IFW-Dresden, Dresden, 01069, Germany

* Corresponding author: Zichao Li and Shengqiang Zhou

E-mail address: zichao.li@hzdr.de and s.zhou@hzdr.de

Abstract: Magnetic skyrmions have been suggested as information carriers for future spintronic devices. As the first material with experimentally confirmed skyrmions, B20-type MnSi was the research focus for decades. Although B20-MnSi films have been successfully grown on Si(111) substrates, there is no report about B20-MnSi films on Si(100) substrates, which would be more preferred for practical applications. In this letter, we present the first preparation of B20-MnSi on Si(100) substrates. It is realized by sub-second solid-state reaction between Mn and Si via flash-lamp annealing at ambient pressure. The regrown layer shows an enhanced Curie temperature of 43 K compared with bulk B20-MnSi. The magnetic skyrmion signature is

proved in our films by magnetic and transport measurements. The millisecond-range flash annealing provides a promising avenue for the fabrication of Si-based skyrmionic devices.

Keyword: B20-MnSi, Si (100) substrates, Flash-lamp annealing, Skyrmions

1. Introduction

In noncentrosymmetric magnetic materials, the Dzyaloshinskii Moriya (DM) interaction can cause spins to arrange non-collinearly [1-3], and together with the ferromagnetic exchange interaction, it results in a whirling domain structure called skyrmions [4-8]. Due to the small size and smaller motion energy for skyrmions, they can be used in new-generation integrated storage devices [9, 10]. Magnetic skyrmions were experimentally observed for the first time in bulk ferromagnetic B20-type MnSi [11]. Afterwards, a lot of effort has been devoted to the growth of B20-MnSi thin films [12-14]. Due to the small lattice mismatch, the films were mostly grown on Si(111) substrates [12-14]. For instance, B20-MnSi films on Si(111) were successfully prepared by molecular beam epitaxy (MBE) [13-15], by solid-state phase epitaxy (SPE) [12, 16], and magnetron sputtering [17]. In most of the cases, MnSi films grown on Si(111) show a Curie temperature of around 43 K, i.e. much higher than the 29.5 K reported for bulk MnSi. However, so far, there has been no report about the formation of B20-MnSi on Si(100) substrate, which is more preferred for spintronic devices due its compatibility with complementary metal-oxide-semiconductor (CMOS) technology. Note that the Si(100) wafer has a higher symmetry than the Si(111) one and its cutting and etching have been well developed [18]. It seems that the growth of B20-MnSi on Si(100) is not possible due to the large mismatch of 16% [19]. Indeed, the $\text{MnSi}_{1.7}$ phase is more easily grown on Si(100) substrates and captures researchers' attention due to its excellent thermoelectric properties [20, 21]. $\text{MnSi}_{1.7}$ films were prepared on Si(100) by SPE [22] and MBE [23]. Furthermore, Wu *et al.* and Kahwaji *et al.* found that B2-MnSi can be formed on Si(100) substrates [24, 25]. However, B2 MnSi cannot host skyrmions since it is centrosymmetric [24]. The absence of B20-MnSi on Si(100) substrates significantly limits the application of skyrmions in integrated spintronics devices. Therefore, it is desirable to search for different growth approaches for B20-MnSi on Si(100) substrates. Xie *et al.* have demonstrated the growth of Mn_5Ge_3 films on Ge(100) by millisecond solid-state reaction, between Mn and Ge via flash-lamp annealing [26]. Note that by normal solid-state reaction Mn_5Ge_3 is more easily formed on Ge(111) substrates [27]. This therefore suggests that a non-equilibrium annealing method could allow for the nucleation of a crystalline phase, which is otherwise not favourable under thermal equilibrium condition.

In this work, we use millisecond flash-lamp annealing induced solid-phase reaction to synthesize B20-MnSi films. We show that the nucleation of B20-MnSi on Si(100) substrates is possible, leading to a continuous polycrystalline thin film, although the MnSi_{1.7} parasitic phase cannot be eliminated. The Curie temperature of the fabricated films, compared to bulk B20-MnSi, increases to around 43 K. The characteristic signature of magnetic skyrmions in our MnSi thin films is proved by magnetization and magneto-transport measurements [13]. The skyrmions can be stabilized from 1000 Oe to 7000 Oe at the whole temperature range below 43 K.

2. Experimental methods

To grow B20-MnSi films, we first deposited Mn films with thicknesses varying from 7 to 30 nm on Si(100) substrates by magnetron sputtering. Afterwards, millisecond flash-lamp annealing (FLA) with 20 ms pulse duration in a continuous N₂ flow was used to heat the sample and to trigger the solid-phase reaction between Mn and Si [28]. During FLA, a bank of capacitors is discharged over a field of flash lamps, producing a light pulse of high intensity. The sample surface will absorb the light and its temperature can reach more than 1000 K within the ms range. Since the pulse duration is only 20 ms, this process results in large heating and cooling rates. Such a non-equilibrium process leads to a very high phase formation speed, making it possible to realize non-equilibrium material phases, like B20-MnSi on Si(100), which is otherwise not possible under thermal equilibrium. The obtained Mn-Si films are around 14-60 nm thick. The topography of the regrown layers was observed by visible-light microscopy. XRD was performed at room temperature by using a Rigaku Smart Lab diffractometer with a Cu-target source. The measurements were done in Bragg-Brentano-geometry with a graphite secondary monochromator and a scintillator detector. Additionally, micro-Raman spectroscopy and transmission electron microscopy (TEM) were employed for microstructure analysis. The micro-Raman experiments were done using a Horiba micro-Raman system with the excitation wavelength of 532 nm and a spot size of 1 μm, and the signal was recorded with a liquid-nitrogen-cooled silicon CCD camera. Bright-field and high-resolution TEM images were recorded with an image-C_s-corrected Titan 80-300 microscope (FEI) operated at an accelerating voltage of 300 kV. High-angle annular dark-field scanning transmission electron microscopy (HAADF-STEM) imaging and spectrum imaging analysis based on energy-dispersive X-ray spectroscopy (EDXS) were performed with a Talos F200X microscope (FEI) operated at 200 kV to obtain the element composition. The magnetic properties of the films were measured by a superconducting quantum interference device equipped with a vibrating sample

magnetometer (SQUID-VSM) with the field parallel (in-plane) to the films. The transport properties of MnSi films were investigated by a Lake Shore Hall measurement system. Magnetic-field (in-plane) dependent resistance was measured between 5 and 45 K using the van der Pauw geometry.

3. Results and Discussions

3.1. Phase identification and structure characterization

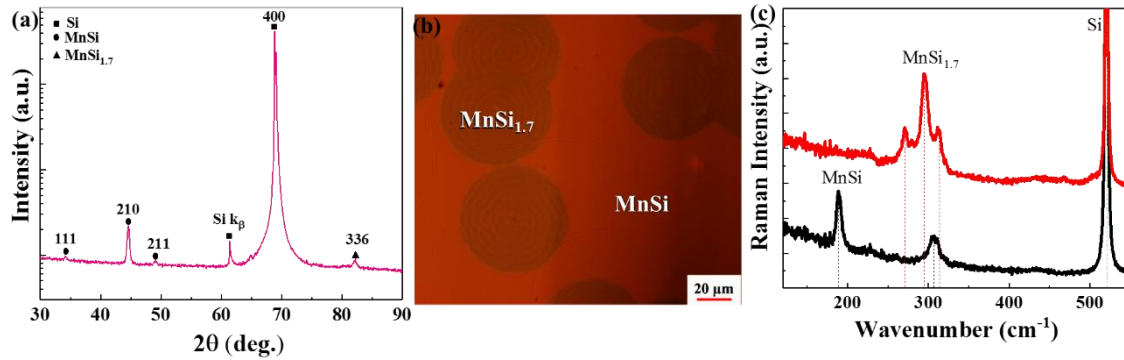


Figure 1. (a) XRD and (b) visible-light microscopy image of the sample annealed from a 30-nm-thick Mn layer on Si(100) substrate. The grey concentric circles are the phase of $\text{MnSi}_{1.7}$ and the featureless area is B20-MnSi. The scale bar is 20 μm . (c) Raman spectra obtained at different positions as shown in (b). For the darker concentric circles and the matrix in-between, the Raman spectra were measured for more than 6 positions. Each matrix position shows the same Raman signal as the black curve, pointing to the B20-MnSi phase. The spectrum of each circular area shows three peaks at around 300 cm^{-1} , consistent with the $\text{MnSi}_{1.7}$ phase.

We first focus on the sample grown from 30 nm Mn on Si(100). Figure 1(a) shows the XRD pattern of this sample. The (400) diffraction peaks of the Si substrate are at 69.5° . The MnSi(111), (210) and (211) Bragg peaks are observed at 34.2° , 44.6° and 49.2° , respectively. According to the powder PDF card (n. 01-081-0484) [23], the MnSi (210) peak is the strongest. Taking into account the intensity ratio between different peaks, the MnSi film grown on Si(100) is of polycrystalline nature. From the XRD pattern, we can confirm the formation of B20-MnSi on Si(100). The parasitic $\text{MnSi}_{1.7}$ phase always coexist with MnSi phase and its (336) Bragg peaks are observed at 82.2° . As shown by a representative visible-light microscopy image of the regrown layer [Fig. 1(b)], there are two different areas: one is composed of darker concentric circles with a diameter of around 60 μm and the other one is the matrix area in-between. To understand the phase formation for these two areas, the corresponding room-temperature Raman spectra are shown in Fig. 1(b). All presented Raman spectra show the peak at around 520.5 cm^{-1} (dashed green lines), which corresponds to the transverse/longitudinal optical (TO/LO) phonon mode in the Si substrate [29]. Additionally, the matrix area shows two well-

separated peaks at about 188 and 307 cm^{-1} (dashed black lines), which correspond to the E or T Raman-active phonon modes in MnSi [30, 31]. In fully relaxed bulk MnSi, these two phonon modes are located at around 194 and 316 cm^{-1} [30, 31]. The shift of the phonon mode positions toward lower wavenumbers indicates the existence of in-plane biaxial tensile strain. The Raman spectrum obtained from the area of the concentric circles exhibits three separated peaks at around $300 \pm 20 \text{ cm}^{-1}$ (dashed red lines). These peaks confirm the formation of the $\text{MnSi}_{1.7}$ phase. These three phonon modes should account for the slightly different neighbourhoods of the Mn–Si bonds in $\text{MnSi}_{1.7}$ [32]. Based on the Raman results, we can conclude that the circular and matrix areas exhibit the $\text{MnSi}_{1.7}$ and B20-MnSi phase, respectively. More specifically, $\text{MnSi}_{1.7}$ is embedded in the B20-MnSi matrix. By rough estimation from the visible-light microscopy images, the areal fraction of the MnSi phase comprises around 45%. A more reliable estimation of this value is given by comparing the saturation magnetization of our films with that of bulk MnSi in the next section. The precipitation of $\text{MnSi}_{1.7}$ in the shape of concentric circles is assumed to be caused by an inhomogeneous temperature distribution or compositional fluctuations [33]. We notice that the formation of $\text{MnSi}_{1.7}$ within the sample of around $10 \times 10 \text{ mm}^2$ is random. Inevitably, some local regions have lower temperature or redundant Si, both favouring the nucleation of $\text{MnSi}_{1.7}$ [28]. However, more investigations are needed for a complete understanding and to control the ratio between MnSi and $\text{MnSi}_{1.7}$.

Figure 2(a) shows a representative cross-sectional bright-field TEM image of the FLA-treated 30-nm-thick Mn layer on Si(100) obtained from the matrix area indicated in Fig. 1(b). Below a 5-to-20-nm-thin amorphous surface film (light-grey with uniform brightness), there is an about 50-nm-thick polycrystalline film which is mainly composed of grains having a height equal to and a lateral extension larger than the film thickness (dark-gray appearance with slightly varying orientation contrast). To further characterize the phase structure of the continuous polycrystalline layer, high-resolution TEM imaging (Fig. 2(b)) combined with fast Fourier transform analysis (Fig. 2(c)) was performed. Taking the B20-type MnSi structure, the diffractogram in Fig. 2(c) can be described by a $[0 \bar{1} 0]$ zone axis pattern (in particular: normal to the growth plane $[3 0 2]$ MnSi is parallel to $[0 0 1]$ Si and in-plane $[0 \bar{1} 0]$ MnSi is parallel to $[1 \bar{1} 0]$ Si). The spatial arrangement of the elements Mn, Si, and O was characterized by EDXS-based analysis in scanning TEM mode and is shown in Fig. 2(d). In particular, Mn and Si are homogeneously distributed within the silicide layer, and the Mn:Si atomic ratio is determined to be close to 1:1. Above the MnSi layer, there is an oxide layer composed of Mn, Si and O. The small oxygen signal within the Mn silicide region is caused by TEM lamella side-wall oxidation during storage in air. For thicker TEM lamella positions, this O signal is even

less pronounced. In summary, TEM analysis confirms the formation of a continuous polycrystalline B20-type MnSi film.

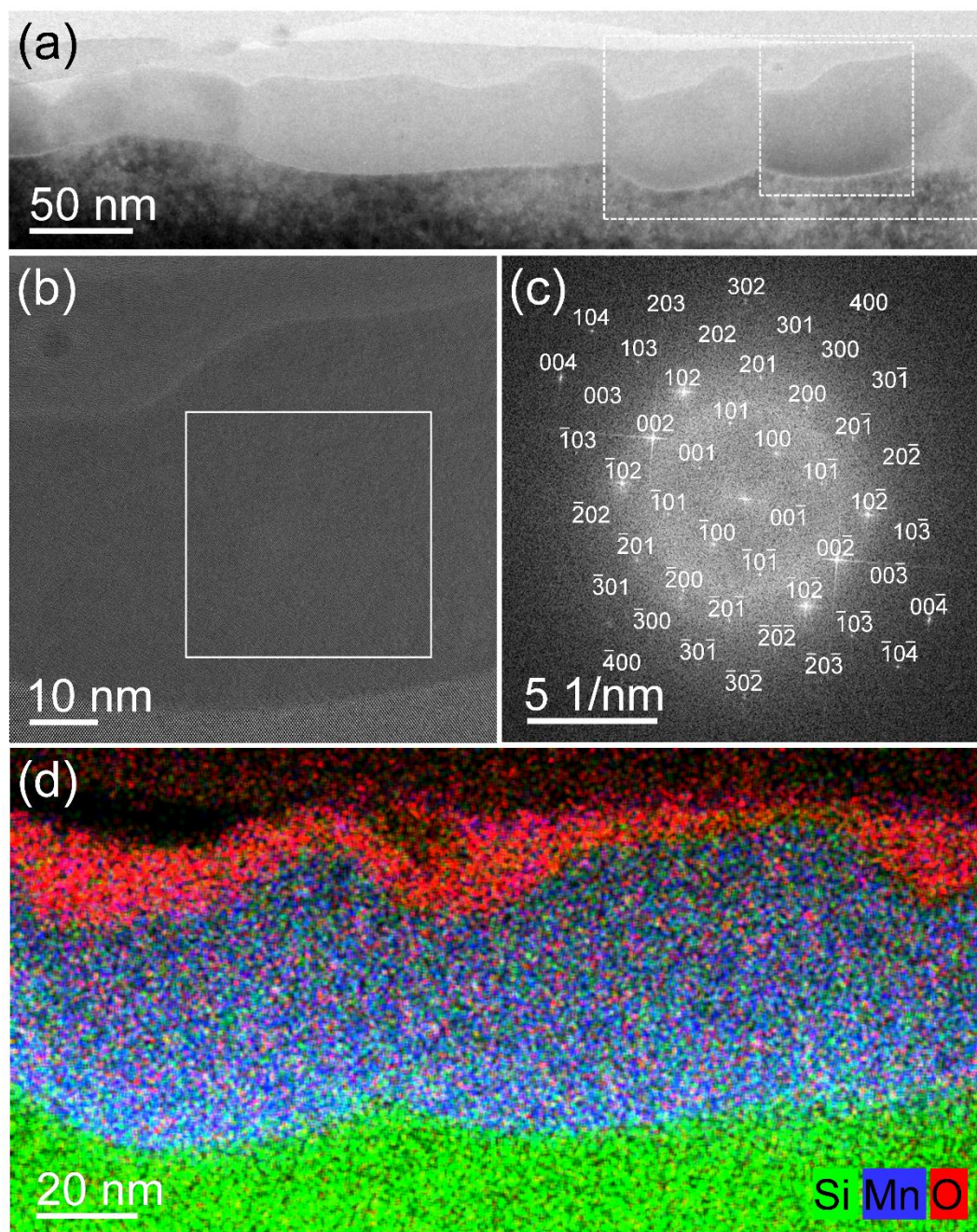


Figure 2. (a) Cross-sectional bright-field TEM image of the FLA-treated 30-nm-thick Mn layer on Si(100) substrate obtained from the matrix area shown in Fig. 1(a). (b) High-resolution TEM image of the area marked with a dashed white square in panel (a). (c) Fast Fourier transform of the region marked with a white square in panel (b) and indexed based on a MnSi $[0 \bar{1} 0]$ zone axis pattern. (d) Superimposed EDXS-based element distributions (blue: manganese, green: silicon, red: oxygen) for the area marked with a white dashed rectangle in panel (a), confirming the presence of a continuous B20-MnSi film.

3.2. Magnetic measurement and skyrmion signature

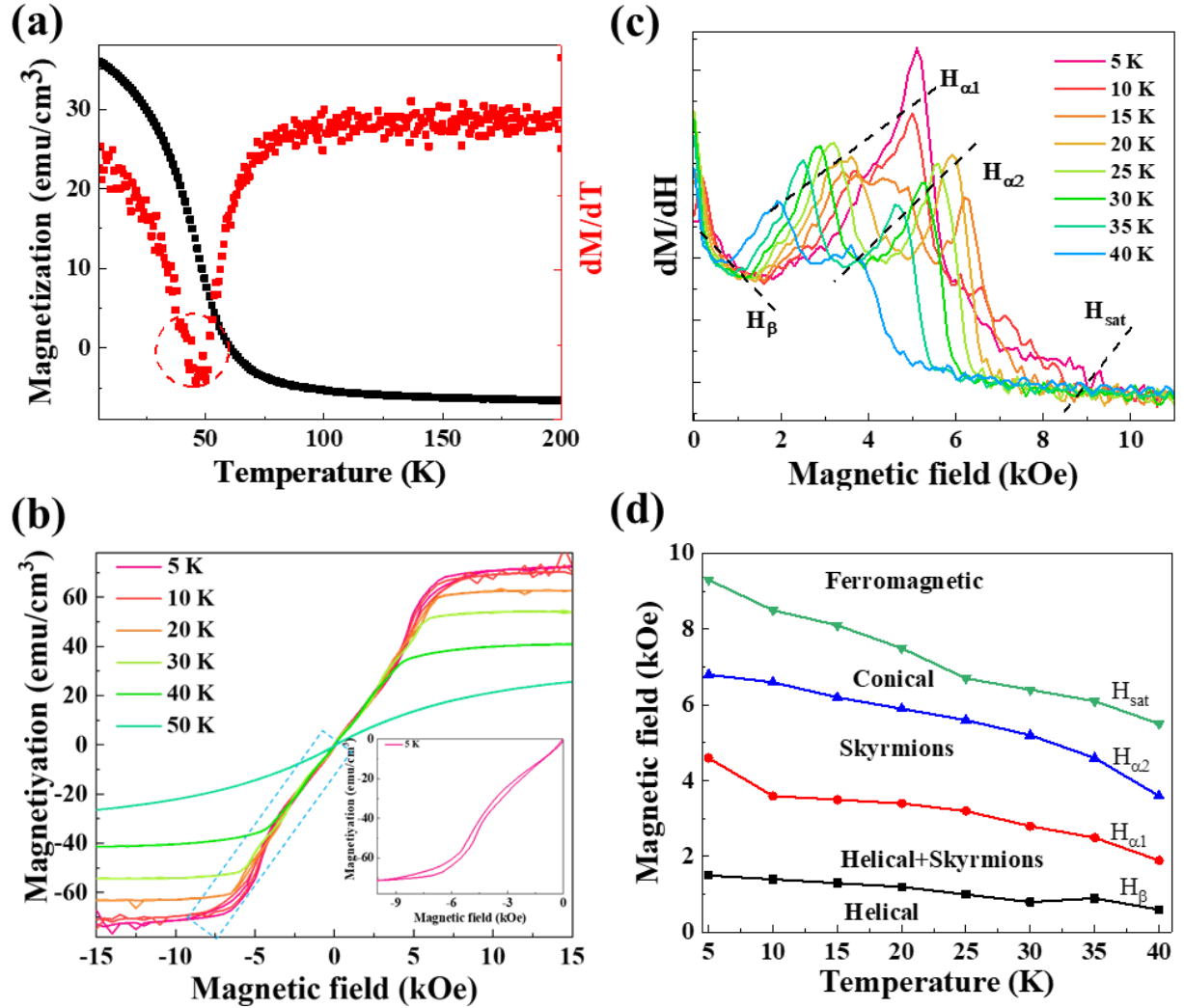


Figure 3. Magnetic properties of B20-MnSi made by solid-state reaction of a 30-nm-thick Mn layer on Si(100) substrate. (a) In-plane saturation magnetization (black squares) and the calculated derivative dM/dT (red squares). The valley of dM/dT at around 43 K indicates the Curie temperature. (b) In-plane M-H curves measured at different temperatures. (c) Static susceptibility in increasing field sweeps for the MnSi film at various temperatures. The black dashed lines in (c) show the shift of transition fields at each temperature. $H_{\alpha 1}$ and $H_{\alpha 2}$ bound the region of stable elliptic skyrmions. The dashed lines define the boundary for metastable helicoids H_{β} and ferromagnetic H_{sat} . (d) Magnetic phase diagram. With increasing temperature, the mentioned magnetic phases formed at lower magnetic fields.

Figure 3(a) displays the temperature-dependent saturation magnetization of the MnSi alloy obtained from the 30-nm-thick Mn layer on Si(100) after FLA. The field was applied along the film surface namely, in-plane. As indicated by the minimum of the derivative dM/dT (red square) curve, the Curie temperature of our B20-MnSi film is 43 K and thus higher than that for bulk MnSi (29.5 K [15]). This Curie temperature enhancement is still under discussion and is very probably caused by strain or defects [34]. It is known that $MnSi_{1.7}$ is a weak itinerant

magnet with a saturation magnetization of $0.012 \mu_B/\text{Mn}$ [35] compared with $0.43 \mu_B/\text{Mn}$ for B20-MnSi [36], which is why the measured magnetization must originate from the B20-MnSi phase. The in-plane MH curves in Fig. 3(b) show multi-hysteresis below the Curie temperature, which arises from the variety of different spin arrangements. To better observe the multi-hysteresis, the insert of Fig. 3(b) is an enlargement of the blue dashed rectangle. Our measurements also indicate that the transition between different magnetic structures occurs within the whole temperature range, not only near the Curie temperature as for bulk MnSi [11]. The saturation magnetization at 5 K is around $72 \text{ emu}/\text{cm}^3$. If we neglect the magnetization of MnSi_{1.7} and compare with the saturation magnetization of $163 \text{ emu}/\text{cm}^3$ for bulk MnSi [11], the MnSi volume fraction in our sample is around 45%. This value is in reasonable agreement with that obtained by calculating areal fraction from Fig. 1(a).

The derivatives of the static magnetization dM/dH are often used to identify the magnetic phase boundaries or critical fields in many skyrmion materials [12, 13, 28]. In Fig. 3(c), the derived dM/dH curves of our films show four critical transition fields, named as H_β , $H_{\alpha 1}$, $H_{\alpha 2}$, and H_{sat} with the dashed lines indicating their shift with temperature. Below H_β , the system stays at its ground helical state. The next apparent peaks at $H_{\alpha 1}$ and $H_{\alpha 2}$ mark the first-order transitions in and out of a new phase with a difference in topology, namely the so-called skyrmion phase [37]. According to this, the region between H_β and $H_{\alpha 1}$ is a transition region, where the ground helical and the skyrmion phase coexist. Above $H_{\alpha 2}$, the skyrmion phase almost vanishes and the system evolves into a conical state, followed by another transition to field-polarized ferromagnetism above the critical field of H_{sat} . Based on the temperature dependency of the transition fields a magnetic phase diagram as shown in Fig. 3(d), can be constructed. With increasing the magnetic field, the Helical, Helical + Skyrmions, Skyrmions, Conical and Ferromagnetism phase emerge in this order [17]. It is in good agreement with other B20-MnSi thin films with in-plane skyrmions which are stabilized by the uniaxial magnetic anisotropy [38, 39]. It is interesting that our B20-MnSi film on Si(100) also hosts skyrmions over a wide temperature and magnetic-field range similar to what has been shown in literature [40, 41]. This enlarged skyrmion stability offers more flexibility in spintronic applications [9, 10, 42].

3.3. Transport measurement and the field-driven evolution of the spin textures

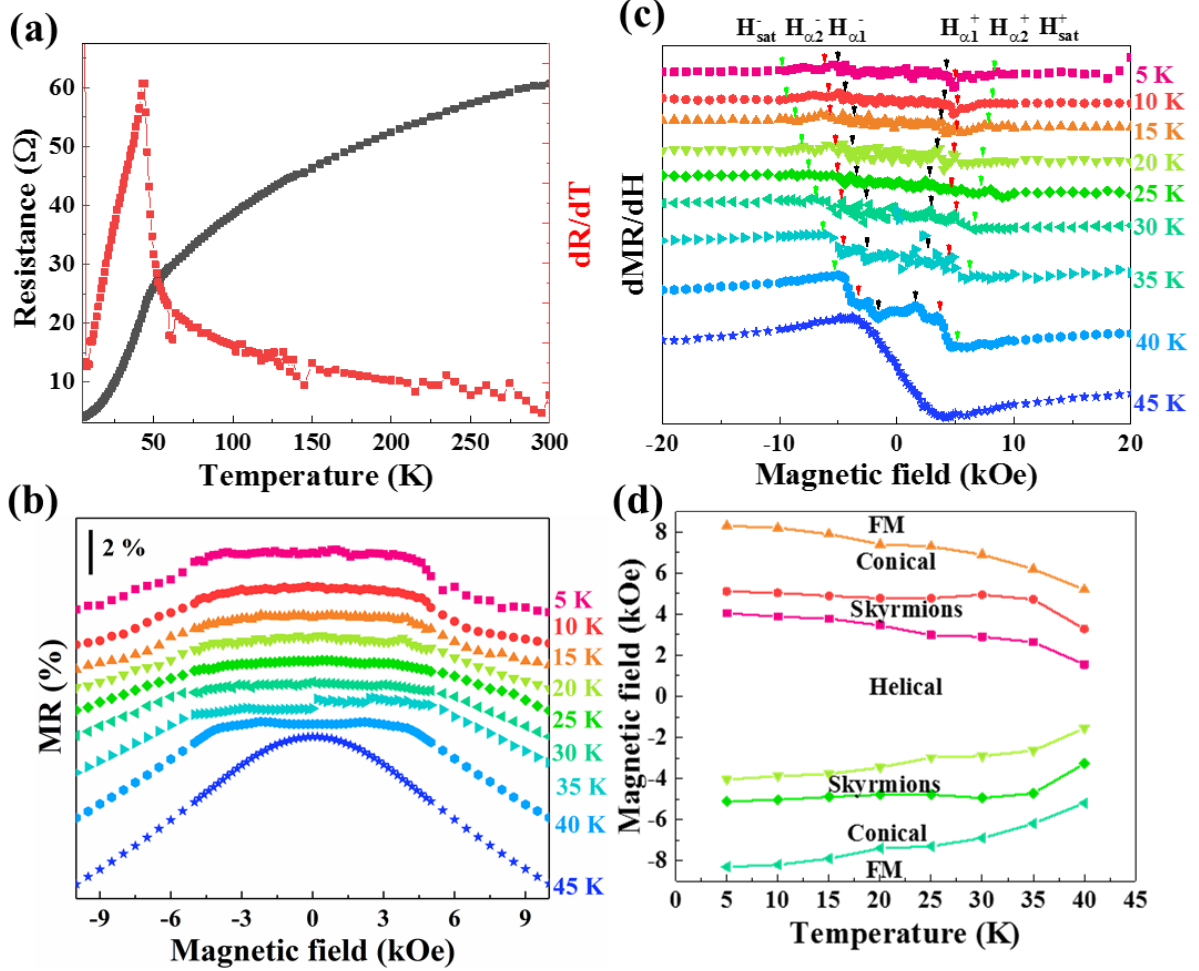


Figure 4. Electrical transport properties of the FLA-treated 30-nm-thick Mn layer on Si(100) substrate. (a) Temperature-dependent resistance (black squares) and calculated dR/dT (red squares). The peak of dR/dT indicates the position of the Curie temperature. (b) Magnetic-field-dependent magnetoresistance at various temperatures. The anomalous plateau disappears at 45 K (above the Curie temperature). (c) Calculated derivative dR/dT from data in panel (b). The black, red, and green arrows stand for the position of H_{c1} , H_{c2} , and H_{sat} , respectively. (d) Magnetic phase diagram of the MnSi film with respect to temperature and magnetic field.

The in-plane electrical resistance of the MnSi film and the calculated dR/dT are shown as a function of temperature in Fig. 4(a). The increase of resistance with temperature clearly indicates the metallic behavior [43] of the MnSi film. Though there are MnSi_{1.7} impurities, the resistance is not affected due to the higher resistivity and semiconducting behavior of MnSi_{1.7}. It seems that the electrons bypass the cylindrical MnSi_{1.7} phase. Thus, the resistance only increases a little compared with pure MnSi samples [28]. The calculated dR/dT in Fig. 4(a) has a peak, indicating the Curie temperature around 43 K, in agreement with the magnetization measurement shown in Fig. 3(a). The magnetoresistance (MR), $MR = \frac{R_H - R_0}{R_0} \times 100\%$ (R_H : resistance under magnetic fields, R_0 : resistance at zero field) of the MnSi film at various temperatures is shown in Fig. 4(b). There is an anomalous plateau with some kinks at low

magnetic fields and below the Curie temperature, which is due to the anomalous topology of skyrmions. Above the Curie temperature, this anomalous plateau disappears [44]. Much more pronounced kink features were reported for Fe_3Sn_2 [8].

We can use the derivative dM/dH from Fig. 4(b) to investigate the field-driven evolution of the spin textures in MnSi. The same approach has been used for MnSi nanowires and other systems [8, 28, 40, 45]. As shown in Fig. 4(c), values for the positive and negative transition fields are denoted by the superscripts “+” and “-”, respectively. With increasing magnetic field, the helimagnetic phase transforms into skyrmions via a first-order phase transition, manifested as peaks at $H_{\alpha 1}$ due to the completely different topological properties between helimagnetic and skyrmion phase. Above the critical field $H_{\alpha 2}$, the system transforms into the conical phase. Skyrmions can be stabilized in the range between $H_{\alpha 1}$ and $H_{\alpha 2}$. H_{sat} is the critical magnetic field, above which MnSi changes into the ferromagnetic state. To better observe the change of the transition fields, the magnetic phase diagram of B20-MnSi obtained by transport measurements is shown in Fig. 4(d). The magnetic skyrmions are stable in a broad field and temperature window, in agreement with the magnetization measurements.

3.4. Skyrmion behavior dependence on the thicknesses of regrown layers

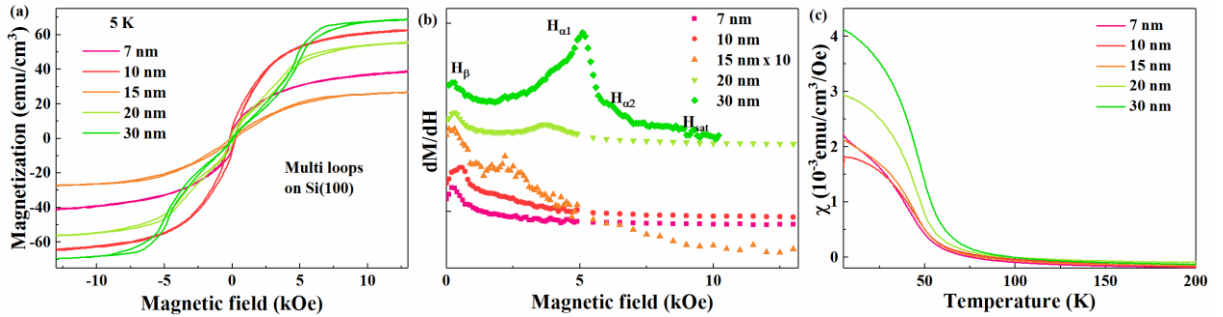


Figure 5. (a) In-plane MH curves (measured at 5 K) after FLA-treatment of Mn/Si(100) samples having different Mn layer thicknesses. The samples annealed from 20- and 30-nm-thick Mn show multi-hysteresis, indicating there is some magnetic phase transitions. (b) The calculated derivative dM/dH of the MH curves from (a). For the sample annealed from 7- and 10-nm-thick Mn, there is only one peak H_{β} , which is the transition from helical to conical state, since the thickness of the regrown layer MnSi is thinner than the theoretical size of MnSi skyrmions. When the Mn layer is thicker than 15 nm, an extra $H_{\alpha 1}$ peak can be detected. To better check the change of the amplitude annealed from 15 nm Mn, the signal is magnified ten times. (c) Magnetic susceptibility χ curves of the samples with different Mn-layer thicknesses.

To check the thickness dependence on the formation of B20-MnSi, Figure 5(a) shows the MH curves obtained from MnSi layers made by solid-state reaction of Mn films with different thicknesses. Since the theoretical size of the skyrmions in MnSi is around 18 nm, the skyrmions

can be detected only when the grain size of MnSi is larger than 18 nm [37]. So, there is no multi-hysteresis, when the deposited Mn is too thin. With increasing the Mn thickness to 15 nm, first traces of the multi-hysteresis originating from the transitions of different magnetic structures can be observed, indicating the existence of magnetic skyrmions in the prepared B20-MnSi films [44]. The MnSi films prepared by ms-range solid-state reaction of 20- and 30-nm-thick Mn layers on Si(100) show obvious multi-hysteresis.

Figure 5(b) shows the calculated derivatives dM/dH . All these curves have a peak H_β at around 300 Oe, which is the transition from the helical to the skyrmionic phase. For samples with 7 and 10 nm Mn, the system changes from helical to conical due to the smaller size of the grains [46, 47]. For thicker films, the neighbor phase is magnetic skyrmion. Since the signal of the sample annealed from 15 nm Mn is very weak compared with other samples, the dM/dH curve is multiplied by 10 to observe the change clearly. Moreover, for the sample annealed from 15, 20 and 30 nm Mn, there is also another peak $H_{\alpha 1}$, where the helical phase completely changes into the skyrmion phase. The peak $H_{\alpha 2}$ is the position, where the metastable skyrmions begin to change into the conical structure. Skyrmions are stabilized in the region from $H_{\alpha 1}$ to $H_{\alpha 2}$. The magnetic state finally changes into ferromagnetism at H_{sat} . The magnetic susceptibility of these samples is shown in Figure 5(c), which shows a similar transition temperature below 50 K and a different magnetic susceptibility due to the different concentrations of the MnSi phase.

3.5. Discussion

The formation of magnetic skyrmions in our MnSi films on Si(100) is indicated by magnetic and magneto-transport measurements. Since the magnetic phase diagram is similar to that of films on Si(111), the formation mechanism of magnetic skyrmions should be the Dzyaloshinskii-Moriya interaction arising from this specific B20 crystal structure. However, atom doping or the second phase could affect the lattice parameters or the anisotropy for stabilizing skyrmions. The film thickness, and hence, the grain size, can also affect the skyrmion behavior. As we show in Figure 5, if the film thickness is too thin, magnetic skyrmions can not be stabilized. We also found that with increasing the fraction of the $\text{MnSi}_{1.7}$ secondary phase, the magnetic field for stabilizing skyrmions becomes smaller. Thus, it might provide a possibility to adjust the skyrmion stabilization window by tuning the content of the second phase.

4. Conclusions

In summary, thin films with the B20-MnSi phase on Si(100) substrates are fabricated for the first time. The nucleation of B20-MnSi is believed to be triggered by the fast solid-state phase reaction between Mn and Si via ms-range flash-lamp annealing. Compared with the corresponding bulk material, the B20-MnSi films made by ms-range annealing show an increased Curie temperature of around 43 K. The magnetic and transport measurements reveal that skyrmions in B20-MnSi on (100) Si made by sub-seconds solid-state reaction are stable within much broader field and temperature windows than bulk MnSi. The parasitic MnSi_{1.7} phase can be further minimized or eliminated by optimizing the annealing conditions, the quality of the deposited Mn film, and its interface with the Si substrate. Our work demonstrates a promising option for the fabrication of B20-type transition metal silicides for integrated and/or hybrid spintronic applications by using Si(100) wafers, which are more preferable for industry applications.

Author contribution statement

Y. Yuan and Z. Li initiated and designed experiments. S. Zhou, L. Rebohle and Z. Li wrote the manuscript from integrating input data and analyses provided from all the authors; V. Begeza, S. Prucnal and Z. Li synthesized samples and performed Raman measurements; T. Naumann and O. Hellwig performed X-ray powder diffraction; Authors acknowledge R. Aniol for TEM specimen preparation; R. Hübner performed TEM measurements; Z. Li performed magnetic and transport measurements. S. Zhou, K. Nielsch and M. Helm supervised the research.

Funding

The author Z. Li (File No. 201707040077) acknowledges the financial support by the China Scholarship Council. Furthermore, the use of the HZDR Ion Beam Center TEM facilities and the funding of TEM Talos by the German Federal Ministry of Education of Research (BMBF), Grant No. 03SF0451, in the framework of HEMCP are acknowledged. The work is also partially supported by the German Research Foundation (DFG, ZH 225/6-1).

Declaration of Competing Interest

The authors declare that they have no known competing financial interests or personal relationships that could have appeared to influence the work reported in this article.

Reference

- [1] A. B. Butenko, A. A. Leonov, U. K. Rößler, A. N. Bogdanov, Stabilization of skyrmion textures by uniaxial distortions in noncentrosymmetric cubic helimagnets, *Phys. Rev. B* 82 (2010) 052403.
- [2] I. E. Dzyaloshinskii, A thermodynamic theory of “weak” ferromagnetism of antiferromagnetics, *Sov. Phys. JETP* 5 (1957) 1259.
- [3] T. Moriya, Anisotropic superexchange interaction and weak ferromagnetism, *Phys. Rev.* 120 (1960) 91.
- [4] X. Z. Yu, Y. Onose, N. Kanazawa, J. H. Park, J. H. Han, Y. Matsui, N. Nagaosa, Y. Tokura, Near room-temperature formation of a skyrmion crystal in thin-films of the helimagnet FeGe, *Nat. Mater.* 10 (2011) 106–109.
- [5] H. C. Wu, P. J. Sun, D. J. Hsieh, H. J. Chen, D. C. Kakarla, L. Z. Deng, C. W. Chu, H. D. Yang, Observation of skyrmion-like magnetism in magnetic Weyl semimetal $\text{Co}_3\text{Sn}_2\text{S}_2$, *Mater. Today Phys.* 12 (2020) 100189.
- [6] M. J. Stolt, S. Schneider, N. Mathur, M. J. Shearer, B. Rellinghaus, K. Nielsch, S. Jin, Electrical Detection and Magnetic Imaging of Stabilized Magnetic Skyrmions in $\text{Fe}_{1-x}\text{Co}_x\text{Ge}$ ($x < 0.1$) Microplates, *Adv. Funct. Mater.* 29 (2019) 1805418.
- [7] Z. Hou, L. Li, C. Liu, X. Gao, Z. Ma, G. Zhou, Y. Peng, M. Yan, X. Zhang, J. Liu, Emergence of room temperature stable skyrmionic bubbles in the rare earth based $\text{RE}\text{Mn}_2\text{Ge}_2$ (RE = Ce, Pr, and Nd) magnets, *Mater. Today Phys.* 17 (2021) 100341.
- [8] Z. Hou, et al. Observation of various and spontaneous magnetic Skyrmionic bubbles at room temperature in a frustrated kagome magnet with uniaxial magnetic anisotropy. *Adv. Mater.* 29 (2017) 1701144.
- [9] S. Bhatti, R. Sbiaa, A. Hirohata, H. Ohno, S. Fukami, S. N. Piramanayagam, Spintronics based random access memory: a review. *Mater. Today* 20 (2017) 530–548.
- [10] A. Fert, N. Reyren, V. Cros, Magnetic Skyrmions: Advances in Physics and Potential Applications, *Nat. Rev. Mater.* 2 (2017) 17031.
- [11] S. Mühlbauer, B. Binz, F. Jonietz, C. Pfleiderer, A. Rosch, A. Neubauer, R. Georgii, P. Böni, Skyrmion lattice in a chiral magnet, *Science* 323 (2009) 915–919.

- [12] Y. Li, N. Kanazawa, X. Z. Yu, A. Tsukazaki, M. Kawasaki, M. Ichikawa, X. F. Jin, F. Kagawa, Y. Tokura, Robust formation of skyrmions and topological Hall effect anomaly in epitaxial thin films of MnSi, *Phys. Rev. Lett.* 110 (2013) 117202.
- [13] M. N. Wilson, E. A. Karhu, A. S. Quigley, U. K. Rößler, A. B. Butenko, A. N. Bogdanov, M. D. Robertson, T. L. Monchesky, Extended elliptic skyrmion gratings in epitaxial MnSi thin films, *Phys. Rev. B* 86 (2012) 144420.
- [14] B. Geisler, P. Kratzer, T. Suzuki, T. Lutz, G. Costantini, K. Kern, Growth mode and atomic structure of MnSi thin films on Si (111), *Phys. Rev. B* 86 (2012) 115428.
- [15] S. L. Zhang, R. Chalasani, A. A. Baker, N.-J. Steinke, A. I. Figueroa, A. Kohn, G. van der Laan, T. Hesjedal, Engineering helimagnetism in MnSi thin films, *AIP Adv.* 6 (2016) 015217.
- [16] E. Karhu, S. Kahwaji, T. L. Monchesky, C. Parsons, M. D. Robertson, C. Maunders, Structure and magnetic properties of MnSi epitaxial thin films, *Phys. Rev. B* 82 (2010) 184417.
- [17] J. López-López, J. M. Gomez-Perez, A. Álvarez, H. B. Vasili, A. C. Komarek, L. E. Hueso, F. Casanova, S. Blanco-Canosa, Spin fluctuations, geometrical size effects, and zero-field topological order in textured MnSi thin films, *Phys. Rev. B* 99 (2019) 144427.
- [18] J.-K. Chang, H. Fang, C. A. Bower, E. Song, X. Yu, J. A. Rogers, Materials and processing approaches for foundry-compatible transient electronics, *Proc. Natl. Acad. Sci. USA* 114 (2017) E5522.
- [19] M. Hortamani, L. Sandratskii, P. Kratzer, I. Mertig, M. Scheffler, Exchange interactions and critical temperature of bulk and thin films of MnSi: A density functional theory study, *Phys. Rev. B* 78 (2008) 104402.
- [20] Q.R. Hou, W. Zhao, Y.B. Chen, Y.J. He, Preparation of n-type nano-scale MnSi_{1.7} films by addition of iron, *Mater. Chem. Phys.* 121 (2010) 103.
- [21] G. Kim, H. Kim, H. Lee, J. Kim, K. Lee, J. W. Roh, W. Lee, Synchronized enhancement of thermoelectric properties of higher manganese silicide by introducing Fe and Co nanoparticles, *Nano Energy* 72 (2020) 104698.
- [22] Y. C. Lian, L. J. Chen, Localized epitaxial growth of MnSi_{1.7} on silicon, *Appl. Phys. Lett.* 48 (1986) 359.

- [23] J. E. Jørgensen S. E. Rasmussen, Refinement of the Structure of MnSi by Powder Diffraction, *Powder Diffr.* 6 (1991) 194.
- [24] H. Wu, M. Hortamani, P. Kratzer, M. Scheffler, First-principles study of ferromagnetism in epitaxial Si-Mn thin films on Si (001), *Phys. Rev. Lett.* 92, 237202 (2004).
- [25] S. Kahwaji, R. A. Gordon, E. D. Crozier, T. L. Monchesky, Local structure and magnetic properties of B2-and B20-like ultrathin Mn films grown on Si (001), *Phys. Rev. B* 85 (2012) 014405.
- [26] Y. Xie, Y. Yuan, M. Wang, C. Xu, R. Hübner, J. Grenzer, Y.-J. Zeng, M. Helm, S. Zhou, S. Prucnal, Epitaxial Mn₅Ge₃ (100) layer on Ge (100) substrates obtained by flash lamp annealing, *Appl. Phys. Lett.* 113 (2018) 222401.
- [27] S. Bechler, M. Kern, H. S. Funk, G. Colston, I. A. Fischer, D. Weisshaupt, M. Myronov, J. Slageren, J. Schulze, Formation of Mn₅Ge₃ by thermal annealing of evaporated Mn on doped Ge on Si (111), *Semicond. Sci. Technol.* 33 (2018) 095008.
- [28] Z. Li, Y. Xie, Y. Yuan, Y. Ji, V. Begeza, L. Cao, R. Hübner, L. Rebohle, M. Helm, K. Nielsch, S. Prucnal, S. Zhou, Phase Selection in Mn-Si Alloys by Fast Solid - State Reaction with Enhanced Skyrmion Stability, *Adv. Funct. Mater.* 31 (2021) 2009723.
- [29] J. Zi, H. Büscher, C. Falter, W. Ludwig, Raman shifts in Si nanocrystals, *Appl. Phys. Lett.* 69 (1996) 200.
- [30] H. M. Either, P. Jaschke, R. Hackl, A. Bauer, M. Gangl, C. Pfleiderer, Raman study of the temperature and magnetic-field dependence of the electronic and lattice properties of MnSi, *Phys. Rev. B* 90 (2014) 024411.
- [31] T. Tite, G. J. Shu, F. C. Chou, Y.-M. Chang, Structural and thermal properties of MnSi single crystal, *Appl. Phys. Lett.* 97 (2010) 031909.
- [32] F. A. Ferri, M. A. Pereira-da-Silva, A. R. Zanatta, Development of the MnSi_{1.7} phase in Mn-containing Si films, *Mater. Chem. Phys.* 129 (2011) 148–153.
- [33] D. Burger, S. Baunack, J. Thomas, S. Oswald, H. Wendrock, L. Rebohle, T. Schumann, W. Skorupa, et al., Evidence for self-organized formation of logarithmic spirals during explosive crystallization of amorphous Ge: Mn layers, *J. Appl. Phys.* 121 (2017) 184901.

- [34] Z. Li, Y. Yuan, V. Begeza, L. Rebohle, M. Helm, K. Nielsch, S. Prucnal, S. Zhou, Curie temperature of MnSi films, submitted (2021).
- [35] U. Gottlieb, A. Sulpice, B. Lambert-Andron, O. Laborde, Magnetic properties of single crystalline Mn₄Si₇, *J. Alloys Compd.* 361 (2003) 13.
- [36] C. Dhital, M. A. Khan, M. Saghayezhian, W. A. Phelan, D. P. Young, R. Y. Jin, J. F. DiTusa, Effect of negative chemical pressure on the prototypical itinerant magnet MnSi, *Phys. Rev. B* 95 (2017) 024407.
- [37] X. Yu, A. Kikkawa, D. Morikawa, K. Shibata, Y. Tokunaga, Y. Taguchi, Y. Tokura, Variation of skyrmion forms and their stability in MnSi thin plates, *Phys. Rev. B* 91 (2015) 054411.
- [38] T. Yokouchi, N. Kanazawa, A. Tsukazaki, Y. Kozuka, A. Kikkawa, Y. Taguchi, M. Kawasaki, M. Ichikawa, F. Kagawa, Y. Tokura, Formation of in-plane skyrmions in epitaxial MnSi thin films as revealed by planar Hall effect, *J. Phys. Soc. Jpn.* 84 (2015) 104708.
- [39] S. A. Meynell, M. N. Wilson, K. L. Krycka, B. J. Kirby, H. Fritzsche, T. L. Monchesky, Neutron study of in-plane skyrmions in MnSi thin films, *Phys. Rev. B* 96 (2017) 054402.
- [40] H. Du, D. Liang, C. Jin, L. Kong, M. J. Stolt, W. Ning, J. Yang, Y. Xing, J. Wang, R. Che, J. Zang, et al., Electrical probing of field-driven cascading quantized transitions of skyrmion cluster states in MnSi nanowires, *Nat. Commun.* 6 (2015) 7637.
- [41] A. Neubauer, C. Pfleiderer, B. Binz, A. Rosch, R. Ritz, P. G. Niklowitz, P. Böni, Topological Hall Effect in the Phase of MnSi, *Phys. Rev. Lett.* 102 (2009) 186602.
- [42] B. Göbel, I. Mertig, O. A. Tretiakov, Beyond skyrmions: Review and perspectives of alternative magnetic quasiparticles. *Phys. Rep.* 895 (2021) 1–28.
- [43] K. Kadowaki, K. Okuda, M. Date, Magnetization and magnetoresistance of MnSi. I, *J. Phys. Soc. Jpn.* 51 (1982) 2433–2438.
- [44] A. Neubauer, C. Pfleiderer, R. Ritz, P. G. Niklowitz, P. Böni, Hall effect and magnetoresistance in MnSi, *Physica B* 404 (2009) 3163.

- [45] S. S. Samatham, V. Ganesan, Critical behavior, universal magnetocaloric, and magnetoresistance scaling of MnSi, *Phys. Rev. B* 95 (2017) 115118.
- [46] E. A. Karhu, U. K. Rößler, A.N. Bogdanov, S. Kahwaji, B. J. Kirby, H. Fritzsche, M. D. Robertson, C. F. Majkrzak, T. L. Monchesky, Chiral modulations and reorientation effects in MnSi thin films, *Phys. Rev. B* 85 (2012) 094429.
- [47] B. Das, B. Balasubramanian, R. Skomski, P. Mukherjee, S. R. Valloppilly, G. C. Hadjipanayis, D. J. Sellmyer, Effect of size confinement on skyrmionic properties of MnSi nanomagnets, *Nanoscale* 10 (2018) 9504.